

SOPHIE velocimetry of *Kepler* transit candidates [★]

IV. KOI-196b: a non-inflated hot-Jupiter with a high albedo

A. Santerne¹, A. S. Bonomo¹, G. Hébrard^{2,3}, M. Deleuil¹, C. Moutou¹, J.-M. Almenara¹, F. Bouchy^{2,3}, and R. F. Díaz^{2,3}

¹ Laboratoire d'Astrophysique de Marseille, Université d'Aix-Marseille & CNRS, 38 rue Frédéric Joliot-Curie, 13388 Marseille cedex 13, France

² Institut d'Astrophysique de Paris, UMR7095 CNRS, Université Pierre & Marie Curie, 98bis boulevard Arago, 75014 Paris, France

³ Observatoire de Haute-Provence, Université d'Aix-Marseille & CNRS, 04870 Saint Michel l'Observatoire, France

Received: 2 August 2011 ; Accepted: 12 September 2011

ABSTRACT

We report the discovery of a new hot-Jupiter, KOI-196b, transiting a solar-type star with an orbital period of $1.855558 \text{ days} \pm 0.6s$ thanks to public photometric data from the *Kepler* space mission and new radial velocity observations obtained by the SOPHIE spectrograph mounted on the 1.93-m telescope at the Observatoire de Haute-Provence, France. The planet KOI-196b, with a radius of $0.841 \pm 0.032 R_{\text{Jup}}$ and a mass of $0.49 \pm 0.09 M_{\text{Jup}}$, orbits a G2V star with $R_{\star} = 0.996 \pm 0.032 R_{\odot}$, $M_{\star} = 0.94 \pm 0.09 M_{\odot}$, $[\text{Fe}/\text{H}] = -0.10 \pm 0.16$ dex, $T_{\text{eff}} = 5660 \pm 100$ K and an age of 7.7 ± 3.4 Gy. KOI-196b is one the rare close-in hot-Jupiters with a radius smaller than Jupiter suggesting a non-inflated planet. The high precision of the *Kepler* photometry permits us to detect the secondary transit with a depth of 64_{-12}^{+10} ppm as well as the optical phase variation. We find a geometric albedo of $A_g = 0.30 \pm 0.08$ which is higher than most of the transiting hot-Jupiters with a measured A_g . Assuming no heat recirculation, we find a day-side temperature of $T_{\text{day}} = 1930 \pm 80$ K. KOI-196b seems to be one of the rare hot-Jupiters located in the short-period hot-Jupiter desert.

Key words. planetary systems – techniques: photometric – techniques: radial velocities – techniques: spectroscopic, star : individual(KOI-196)

1. Introduction

Since 2007, thanks to the exoplanet-dedicated space missions *CoRoT* (Baglin et al. 2006) and *Kepler* (Borucki et al. 2010b), the scientific community has access to very high precision photometry, down to a few tens of ppm with times series up to a few years. This has led to the exciting discoveries of the super-Earths *CoRoT-7b* (Léger et al. 2009; Queloz et al. 2009) and its twin *Kepler-10b* (Batalha et al. 2011), the multi-planetary systems *Kepler-9* (Holman et al. 2010) and *Kepler-11* (Lissauer et al. 2011) and the long-period giant planet *CoRoT-9b* (Deeg et al. 2010). Long space-based time series allow us to reach a very accurate characterization of the planetary systems, especially when stellar parameters can be determined by asteroseismology (e.g. Batalha et al. 2011; Demory et al. 2011).

Moreover, high-precision space-based photometry permits us to find also very small effects, such as the planetary occultation (e.g. Alonso et al. 2009a), i.e. when the planet passes behind its host star, as well as the phase variation of the planet, i.e. the variation in brightness as the dayside of the planet rotates into view. The latter was found in the optical for *CoRoT-1b* (Snellen et al. 2009), *HAT-P-7b* (Borucki et al. 2009; Welsh et al. 2010), *Kepler-7b* (Demory et al. 2011) and the super-Earth *Kepler-10b* (Batalha et al. 2011).

The first six months of *Kepler* data have permitted identifying 1235 planetary candidates around 997 stars (Borucki et al. 2011) including twenty one fully characterized planets (with measured radius and mass) (e.g. Borucki et al. 2010a; Latham et al. 2010; Santerne et al. 2011; Bouchy et al. 2011) and three confirmed planets without measured mass (e.g. Torres et al. 2011). Out of the remaining candidates, we have selected a few candidates around stars brighter than the *Kepler* magnitude $K_p \sim 14.7$ to be followed up with the SOPHIE spectrograph (Observatoire de Haute-Provence, France). One of these is the new exoplanet KOI-196b. In this paper we report its discovery (Sect. 2 & 3) and the system characterization (Sect. 4) including an estimate of the planetary albedo and day-side temperature (Sect. 5) thanks to the observation of the secondary and phase variation (Sect. 2.3). Finally, we discuss KOI-196b and compared it to other transiting planets in terms of mass, radius, period and day-side temperature (Sect. 6).

2. *Kepler* observations

The *Kepler* Object of Interest KOI-196 has been observed by *Kepler* since May 13, 2009 in long-cadence mode (temporal sampling of ~ 29.4 min). The various identifiers (ID) of this target, including coordinates and magnitudes are reported in Table 1. At the time of writing of the present paper, only quarters 1 & 2 (Q1 & Q2) data sets are publicly available on the MAST archive¹. They account for a total of 5 993 photometric measurements. 285 points were discarded by the *Kepler* pipeline (Jenkins et al. 2010) as they are affected by instrumental effects.

Send offprint requests to: Alexandre Santerne
e-mail: alexandre.santerne@oamp.fr

[★] Based on observations made with SOPHIE on the 1.93-m telescope at Observatoire de Haute-Provence (CNRS), France

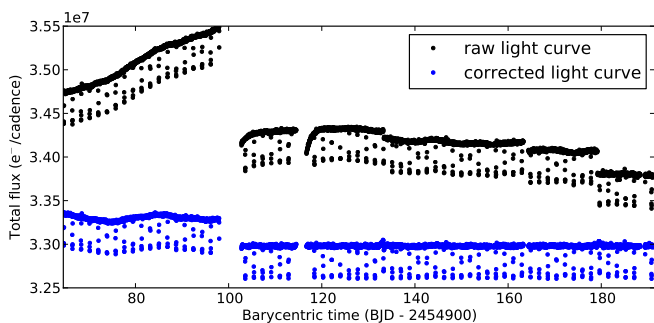
¹ <http://archive.stsci.edu/>

Table 1. KOI-196 IDs, coordinates and magnitudes

<i>Kepler</i> Input Catalog (KIC)	9410930
<i>Kepler</i> Object of Interest (KOI)	196.01
2MASS ID	19380317+4558539
Right Ascension (J2000)	19 38 03.19
Declinaison (J2000)	45 58 53.76
<i>Kepler</i> magnitude ^(a)	14.465 ± 0.02
$g^{(a)}$	14.996
$r^{(a)}$	14.410
$i^{(a)}$	14.238
$z^{(a)}$	14.182 ± 0.030
$J^{(b)}$	13.262 ± 0.022
$H^{(b)}$	12.938 ± 0.024
$K^{(b)}$	12.892 ± 0.028
$E(B - V)^{(a)}$	0.114 ± 0.100

^(a) from the *Kepler* Input Catalog. ^(b) from 2MASS catalog.

The 5708 remaining photometric measurements are displayed in Fig. 1. Transits with a period of ~ 1.8 days and a depth of $\sim 1\%$ are clearly visible in the light-curve of KOI-196 showing no prominent features related to magnetic activity.

**Fig. 1.** Raw and corrected light curve of KOI-196 as provided by the MAST database.

2.1. Contamination correction

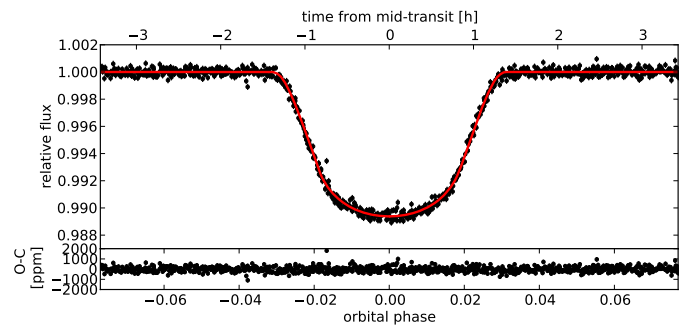
For the following studies, we used the raw light curve (hereafter LC) instead of the PDC-corrected light curve as recommended by the *Kepler* Team². The flux of several nearby stars contaminates the target one and has to be taken into account when working with the raw LC. We estimated the contamination value by comparing the raw and the PDC-corrected LC following the same methodology as described in Bouchy et al. (2011). We calculated it separately for each quarters. We find a contamination value of $5.1\% \pm 0.06\%$ for Q1 and $3.3\% \pm 0.04\%$ for Q2 which is in good agreement with the values for seasons 3 and 0, respectively, available on the MAST database (see also Sect. 2.4).

2.2. Primary transit modeling

Before performing the transit modeling, we normalized the transits by fitting a parabola to the ~ 11 h intervals of the LC before the ingress and after the egress of each transit in order to correct for any local variations. We discarded one of the 63 available transits occurring at BJD \sim 2455033.3 and is affected by one of the discontinuities seen in the LC (see Fig. 1).

Transit modeling was performed following the formalism of Giménez (2006) fixing the eccentricity to zero (see Sect. 2.3). The seven free parameters used in the transit modeling were the orbital period P , the epoch of the first transit t_0 , the transit duration T_{14} , the planet to star radii ratio $k = R_p/R_*$, the orbital inclination I , and the two limb-darkening coefficients $u_+ = u_a + u_b$ and $u_- = u_a - u_b$.

The best-fit of the primary transit was performed using the algorithm AMOEBA (Press et al. 1992) and changing the initial parameters with a Monte Carlo to find the global minimum of the χ^2 . We followed the procedure described in Kipping (2010) to take the long cadence rate of the *Kepler* LC into account: the χ^2 was computed by binning a five-times oversampled model LC within the long cadence rate of *Kepler* and compared to the data. The phase-folded transit and the best-fit model as well as the residuals between the observations and the model are shown in Fig. 2. We used a bootstrap procedure to estimate the uncertainties which consist in generating synthetic data sets shifting the residuals from the best-fit, adding them back to the best-fit model LC and fitting once again the data. We finally determined the $1-\sigma$ uncertainty as the 68% confidence interval defined as 16% above the upper (and below the lower) confidence limit of the cumulative probability. The parameters of the best-fit model and their $1-\sigma$ uncertainties are reported in Table 2.

**Fig. 2.** Phase-folded unbinned light curve of the KOI-196b transit with its best-fit model (top panel) and residuals (bottom panel).

2.3. Modeling the occultation and orbital phase variations

Space-based high-precision photometry has shown its capability to detect planetary occultation and phase variation for close-in planets (e.g. Alonso et al. 2009a,b; Snellen et al. 2009, 2010; Borucki et al. 2009; Demory et al. 2011). Even if KOI-196 is faint, we cleaned the LC to try to detect both effects. To that purpose, we first removed all the transits from the raw LC corrected from the contamination (Sect. 2.1). We then

² <http://keplergo.arc.nasa.gov/PipelinePDC.shtml>

corrected for long-term trends separately in the Q1 and the two first subsets of the Q2 data between BJD 2455000.0 and 2455033.3, by fitting polynomials of the 8th order. For the other subsets of the Q2 LC, we just removed the offsets around each discontinuity. We finally de-trended the whole LC using a sliding median with a window of 1.5 times the orbital period, taking care of mirroring the LC at the beginning and the end. This method leads to a total dispersion of 243ppm after a 3- σ clipping. The obtained LC, phase-folded at the transit ephemeris is displayed in Fig. 3 and clearly shows an occultation as well as orbital phase variations. We also tested different sliding median windows between $\sim 1.5 \cdot P$ and $\sim 2.5 \cdot P$ and got the same result with a slightly larger dispersion. As expected, windows with extensions less than the orbital period significantly reduce the amplitude of the phase variations we are searching for and thus, our choice of $1.5 \cdot P$ is the best compromise between preserving the signal we want to detect and minimizing the RMS of the residuals.

We characterized the occultation and phase variations using the formalism proposed by Snellen et al. (2009). To model the occultation, we fixed the values of the orbital period, the epoch of transit, the transit duration, the radii ratio and the inclination to those derived by the transit modeling but without introducing the LD coefficient, as the planet is passing behind the star. We first binned the LC to 0.02 in phase (inset of Fig. 3) and fitted an out-of-transit model with four free parameters: the phase of the secondary eclipse ϕ_{occ} , the contrast between the planet day-side and stellar flux R_{day} , the ratio of the night-side to day-side flux $F_{\text{N/D}}$ and the relative stellar brightness z_{lev} (Snellen et al. 2009). As for the transit modeling, we found the best-fit solution using the algorithm AMOEBA and changing the initial parameters with a Monte Carlo method to determine the global minimum of the χ^2 . We also oversampled the model to take the bin size into account. We found the phase of the secondary eclipse to be $\phi_{\text{occ}} = 0.499^{+0.004}_{-0.017}$ which allow us to constrain $e \cos \omega = -0.002^{+0.006}_{-0.017}$ (Giménez 2009). Thus, we assumed that the eccentricity of KOI-196b is zero. Then, we performed again an out-of-transit modeling to the unbinned LC, fixing the phase of the occultation to 0.5 and allowing the three remaining parameters to vary. We computed the χ^2 by comparing the data with a five-times oversampled model binned at the *Kepler* cadence rate. Indeed, we expected that not oversampling the model could lead to an underestimation of the occultation depth. The best fit corresponding to the global minimum of the χ^2 is plotted in Fig. 3 and the derived parameters are displayed in Table 2. One- σ uncertainties were determined using a bootstrap procedure as for the primary transit (see Sect. 2.2).

2.4. Centroid motion

In order to test whether the centroid behaviour was compatible with the target's vicinity (Batalha et al. 2010), we performed simple 2D simulations of the photometric properties of KOI-196 and its five neighbours located less than $0.3'$ from KOI-196 and described in the MAST archive. All of them are fainter than $K_p = 16.2$. We used circular apertures instead of the actual *Kepler* PSF; this assumption should impact only the farthest contaminants. It results that all configurations where one of the neighbours produces the transit are discarded, since this would imply a shift in the X and/or Y directions of 2 to 20 mpixels in absolute value. In our simulations, when KOI-196 is the transit-

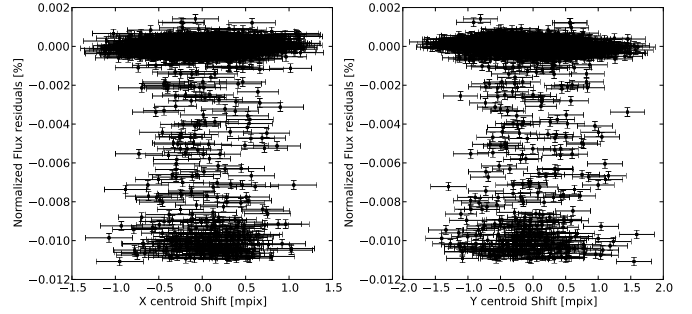


Fig. 4. Rain plots showing X (left panel) and Y (right panel) shift of the centroid during the transit as function of the normalized flux residuals.

ing star, we still find a little centroid shift of 1-2 mpixels. The observed centroid positions have a mean value of 0 in both directions, with 1- σ errors of 0.4 and 0.6 mpix in X and Y, respectively (see Fig 4). The simple simulations of the photocenter of KOI-196 being disturbed by its neighbours are therefore in agreement with the observations, within 2- σ .

3. SOPHIE observations

3.1. Observations and data reduction

We performed spectroscopic follow-up observations on the target KOI-196 with the SOPHIE spectrograph (Perruchot et al. 2008; Bouchy et al. 2009c) mounted on the 1.93-m telescope at Observatoire de Haute-Provence, France. We acquired twelve high-resolution spectra from March 25 to July 29, 2011³ using the High Efficiency mode ($R \sim 39\,000$ at 550nm) of SOPHIE and the slow CCD read-out mode in order to minimize the instrumental and photon noise. Observations were done by keeping the SNR of the spectra constant in order to minimize the charge transfer inefficiency effect (Bouchy et al. 2009a). Spectra were reduced with the online standard pipeline and radial velocities were obtained by computing the weighted cross-correlation function (CCF) of the spectra with a numerical spectral mask of a G2V star (Baranne et al. 1996; Pepe et al. 2002). Three of the spectra were significantly affected by the Moon's scattered light. Their corresponding radial velocity were corrected using the same technique as in Santerne et al. (2011) and Bonomo et al. (2010). Other two spectra were slightly affected by the Moon scattered light and were not corrected since the Moon light affected the measurement at the level of a few m s^{-1} , which is compatible with the noise added by the correction.

These radial velocities are listed in Table 3 and displayed in Fig. 5 & 6. They show a clear variation compatible with the reflex motion of the parent star KOI-196 due to a planetary companion in phase with the *Kepler* ephemeris. Since we found a secondary eclipse at phase ~ 0.5 (c.f. Sect. 2.3) and that circularization time-scales for such close-in planets are very short (Mardling 2007), we assumed the orbit to be circular and fitted a corresponding keplerian to the data. We found a best fit with a semi-amplitude $K = 85 \pm 11 \text{ m s}^{-1}$ and a $\sigma_{\text{O-C}} = 24 \text{ m s}^{-1}$ which is comparable with the mean radial velocity uncertainty

³ prog. ID: 11A.PNP.MOUT

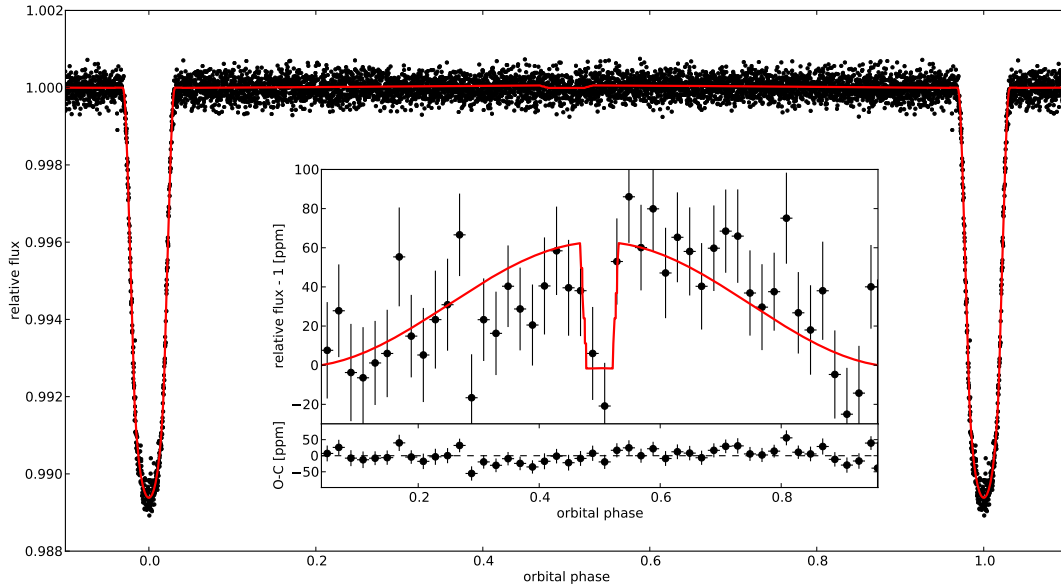


Fig. 3. Unbinned phase-folded light curve of KOI-196 with the best-fit model. The inset displays a zoom of the out-of-transit LC binned to 0.02 in phase with the best-fit model of the planet phase variation and occultation (inset, top panel) and its residuals (inset, bottom panel). Out-of-transit residuals binned to 0.02 in phase have a dispersion of 22 ppm.

$$\langle \sigma_{\text{TV}} \rangle = 20 \text{ m s}^{-1}.$$

From the SOPHIE CCF parameters, one can estimate the $\nu \sin i_*$ and $[\text{Fe}/\text{H}]$ using equations described in Boisse et al. (2010). Using the FWHM and contrast of the CCF and assuming $(B - V) = 0.63$, we find a $\nu \sin i_* = 4.1 \pm 1.0 \text{ km s}^{-1}$ and $[\text{Fe}/\text{H}] = -0.17 \pm 0.15 \text{ dex}$.

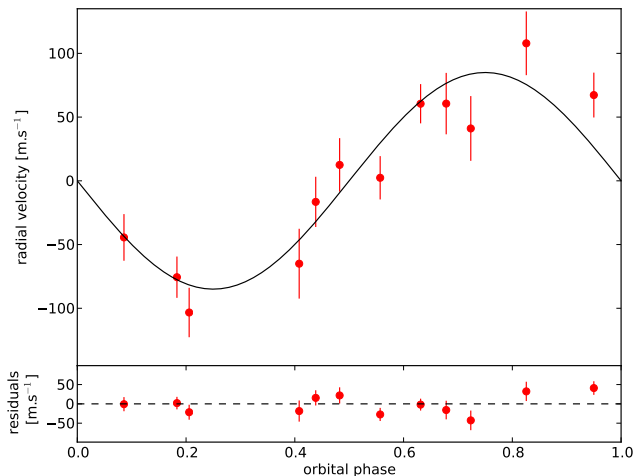


Fig. 5. Phase-folded radial velocity curve with our best-fit (top panel) and residuals (bottom panel).

3.2. Blend analysis

If the RV signal is mimicked by a diluted blended binary one can expect to see some correlation between the bisector span

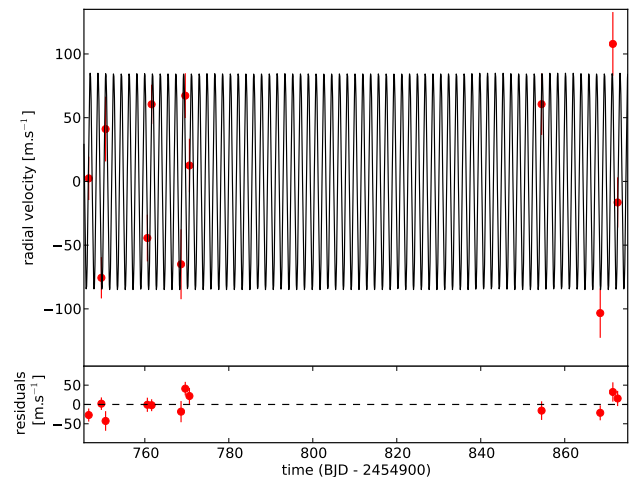


Fig. 6. Radial velocity curve with our best-fit (top panel) and residuals (bottom panel).

and radial velocities or different RV amplitude when processing the CCF with different spectral type mask templates (Bouchy et al. 2009b). We first fitted the different RV datasets processed with K5 and F0 masks with a circular orbit model and found that $K_{\text{K5}} = 84 \pm 11 \text{ m s}^{-1}$, $\sigma_{\text{O-C}} = 20 \text{ m s}^{-1}$ and $K_{\text{F0}} = 85 \pm 14 \text{ m s}^{-1}$, $\sigma_{\text{O-C}} = 32 \text{ m s}^{-1}$ which is in good agreement with the amplitude derived with the G2 mask.

Bisector span is also a key CCF diagnostics which is very sensitive to stellar activity and additional blended stellar component (Queloz et al. 2001; Bouchy et al. 2009b, Santerne et al., in prep.). In order to assess the possibility that the radial velocity variations are not caused by a blended binary, we measured

the bisector spans which are listed in Table 3 and plotted in Fig. 7. They do not reveal any significant variation within $1\text{-}\sigma$. Moreover, neither radial velocities, nor their residuals present a significant correlation with the bisector. These two checks allow us to secure the planetary nature of KOI-196b.

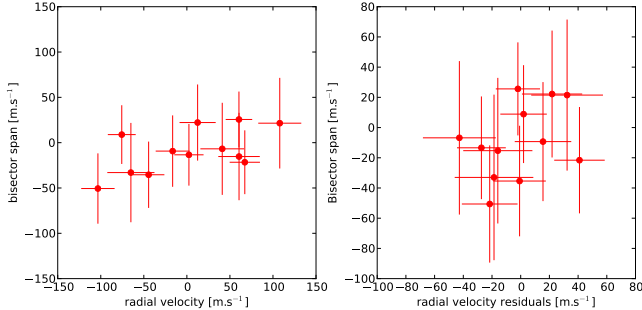


Fig. 7. CCF bisector as function of radial velocity (left panel) and radial velocity residuals (right panel).

4. System parameters

To perform the spectral analysis of the KOI-196b host star, we used the four SOPHIE spectra took before June 2011 that were not affected by Moon reflected light at the time of the observations. Since such individual spectra have too low signal-to-noise ratio to allow a proper analysis, we co-added them after correcting of the barycentric Earth radial velocity projected through the line of sight and of the star's one. The resulting co-added spectrum has a signal-to-noise of 46 per element of resolution at the continuum at 5550 \AA with a spectral resolution of ~ 39000 . We used the semi-automatic software package VWA (Bruntt et al. 2002, 2008) to derive the stellar photospheric parameters as described in Bruntt et al. (2010).

Using the same methodology as presented in Bruntt et al. (2010) we derived the projected rotational velocity $\nu \sin i_\star = 4.5 \pm 1.5 \text{ km s}^{-1}$ from the analysis of a few isolated spectral lines. This value is in good agreement with the $\nu \sin i_\star$ estimated from the CCF assumed that the true value of the $\nu \sin i_\star$ could be even lower since we are here limited by the spectral resolution of SOPHIE. For the atmospheric parameters we found $T_{\text{eff}} = 5660 \pm 100 \text{ K}$, $[\text{Fe}/\text{H}] = -0.09 \pm 0.16 \text{ dex}$ and $\log g = 4.35 \pm 0.2$. It is known that the $\log g$ is the most uncertain parameter derived from spectral analysis. The quite low signal-to-noise of our co-added spectrum combined with the moderate spectral resolution do not permit us to estimate this parameter more accurately. The derived stellar parameters are reported in Table 2. They are in a good agreement within the error bars, with the estimates published in Borucki et al. (2011) $T_{\text{eff}} = 5585 \text{ K}$ and $\log g = 4.51$ with uncertainties up to 30%.

From infrared photometry J and K available in the 2MASS archive, we computed the photometric $T_{\text{eff}} = 6000 \pm 150 \text{ K}$ following Casagrande et al. (2010), assuming $[\text{Fe}/\text{H}]$ of -0.10 dex and taking a reddening of $E(J-K) = 0.059$ (Cardelli et al. 1989) into account. This photometric estimation is at $2\text{-}\sigma$ from the one determined by spectral analysis and might be explained by

an upper value of the reddening provided in the MAST database.

Finally, we used the stellar density derived by the transit modeling combined with the T_{eff} from the spectral analysis to determine the star's fundamental parameters in the $(T_{\text{eff}}, M_\star^{1/3}/R_\star)$ space. The position of the star in the H-R. diagram was compared to STAREVOL evolution tracks (Turck-Chièze et al. 2010) minimizing the χ^2 as described in Santerne et al. (2011). We found a main-sequence solution with $M_\star = 0.94 \pm 0.09 M_\odot$ and $R_\star = 0.966 \pm 0.032 R_\odot$. Main-sequence solutions are consistent with the absence of Lithium in the spectrum of the star and the low $\nu \sin i_\star$ value we derived. We note that the inferred gravity surface $\log g = 4.44 \pm 0.10$ is in good agreement with the spectroscopic value within $1\text{-}\sigma$ as well as the one published by Borucki et al. (2011): $\log g = 4.5$. This solution led to an age of $7.7 \pm 3.4 \text{ Gyr}$.

These stellar parameters yield limb darkening coefficients in the *Kepler* bandpass of $u_+ = 0.66 \pm 0.03$ and $u_- = 0.15 \pm 0.03$ (using interpolated values from Sing 2010). They are in good agreement with those obtained from the transit modeling within $2\text{-}\sigma$ and $1\text{-}\sigma$ for u_+ and u_- , respectively.

From the adopted stellar fundamental parameters, combined with results from the transit modeling and the analysis of the radial velocity observations, we find a mass and a radius of the planet of $M_p = 0.49 \pm 0.09 M_{\text{Jup}}$ and $R_p = 0.841 \pm 0.032 R_{\text{Jup}}$. The inferred mean density of the planet is $\rho_p = 1.02 \pm 0.18 \text{ g.cm}^{-3}$.

5. Geometric albedo characterization

The high accuracy of the *Kepler* photometry as well as the large number of orbital periods covered during Q1 & Q2 allowed us to clearly detect both the secondary transit and the phase variation in the optical (a $5\text{-}\sigma$ detection, see Sect. 2.3). Assuming a pure reflecting planet without thermal emission we found a geometric albedo of $A_g = 0.33^{+0.07}_{-0.08}$ in the *Kepler* bandpass (Rowe et al. 2006). Even in the optical, part of the observed light from the planet could be due to thermal emission (López-Morales & Seager 2007; Snellen et al. 2009). The observed occultation depth is thus a combination of the reflected light and the thermal emission:

$$\delta_{\text{occ}} = \frac{F_{p_{\text{th}}}}{F_\star} + \frac{F_{p_{\text{ref}}}}{F_\star} \quad (1)$$

where $F_{p_{\text{th}}}$ is the thermal flux generated by the planet and $F_{p_{\text{ref}}}$ is the reflected light. Using eq. 14 in Rowe et al. (2006) the reflected component of the occultation depth expressed as:

$$\frac{F_{p_{\text{ref}}}}{F_\star} = A_g \left(\frac{R_p}{a} \right)^2 \quad (2)$$

for which R_p/a is well constrained by the modeling of the primary transit.

To estimate the fraction of thermal emission that contributes to the planetary occultation, we computed the ratio between the flux of the star and the expected thermal flux of the planet assuming a blackbody emission. If the planet is tidally locked, its

Table 2. Star and planet parameters.

<i>Ephemeris</i>	
Planet orbital period P [days]	1.855558 ± 7.10^{-6}
Transit epoch T_{tr} [BJD - 2454900]	70.1803 ± 0.0003
<i>Results from radial velocity observations</i>	
Orbital eccentricity e	0 (fixed)
Semi-amplitude K [m s $^{-1}$]	85 ± 11
Systemic velocity V_r [km s $^{-1}$]	-27.066 ± 0.007
O-C residuals [m s $^{-1}$]	24
<i>Fitted transit parameters</i>	
Radius ratio $k = R_p/R_\star$	0.0895 ± 0.0019
Orbital inclination I [deg]	88.3 ± 0.7
transit duration T_{14} [h]	2.376 ± 0.048
limb darkening coefficient u_+	0.98 ± 0.17
limb darkening coefficient u_-	0.16 ± 0.20
<i>Deduced transit parameters</i>	
Scaled semi-major axis a/R_\star	6.43 ± 0.05
Impact parameter b	0.19 ± 0.07
$M_\star^{1/3}/R_\star$ [solar units]	1.012 ± 0.009
Stellar density ρ_\star [g cm $^{-3}$]	1.46 ± 0.04
<i>Fitted and deduced Out-of-Transit parameters</i>	
phase of secondary transit ϕ_{occ}	$0.499^{+0.004}_{-0.011}$
planet day-side to stellar flux ratio R_{day} [ppm]	64^{+10}_{-12}
planet night-side to day-side flux ratio $F_{N/D}$	< 0.24
relative stellar brightness z_{lev}	0.99993 ± 0.00001
$e \cos \omega$	$-0.002^{+0.006}_{-0.017}$
<i>Spectroscopic parameters</i>	
Effective temperature T_{eff} [K]	5660 ± 100
Metallicity [Fe/H] [dex]	-0.09 ± 0.16
Stellar rotational velocity $v \sin i_\star$ [km s $^{-1}$]	4.5 ± 1.5
Spectral type	G2V
<i>Stellar physical parameters from combined analysis</i>	
Star mass M_\star [M_\odot]	0.94 ± 0.09
Star radius R_\star [R_\odot]	0.966 ± 0.032
Surface gravity $\log g^a$ [dex]	4.44 ± 0.10
Age of the star t [Gy]	7.7 ± 3.4
Distance of the system [pc]	730 ± 70
<i>Planetary physical parameters from combined analysis</i>	
Orbital semi-major axis a^b [AU]	0.029 ± 0.001
Planet mass M_p [M_{Jup}]	0.49 ± 0.09
Planet radius R_p [R_{Jup}]	0.841 ± 0.032
Planet density ρ_p [g cm $^{-3}$]	1.02 ± 0.18
Geometric albedo A_g	0.30 ± 0.08
Day-side temperature T_{day} [K]	1930 ± 80

^a derived from M_\star and R_\star .

^b derived from a/R_\star and R_\star .

^c considering no atmospheric thermal circulation.

day-side temperature can be calculated using the following expression (Cowan & Agol 2011):

$$T_d = T_{eff} \sqrt{\frac{R_\star}{a}} (1 - A_B)^{\frac{1}{4}} \left[\frac{2}{3} - \frac{5}{12} \varepsilon \right]^{\frac{1}{4}} \quad (3)$$

where the Bond albedo A_B is fixed to zero assuming black-body emission and ε is the circulation efficiency that is allowed to vary from $\varepsilon = 1$ for a full redistribution of the energy budget

from the day-side towards the night-side to $\varepsilon = 0$ for no heat circulation in the atmosphere.

We used the Castelli & Kurucz (2004) atmospheric model⁴, S_λ^{CK} , of a solar-like star to estimate the stellar flux and integrated over the *Kepler* bandpass Ω_λ ⁵. Then, we integrated the Planck function at the day-side brightness temperature T_d of the planet over the *Kepler* bandpass. The occultation depth due to thermal emission is the ratio between the two fluxes, multiplied by the surface areas of the planet and the star, respectively :

$$\frac{F_{p,th}}{F_\star} = \pi k^2 \frac{\int_\lambda \frac{2hc^2}{\lambda^5} \left[\exp\left(\frac{hc}{k_B \lambda T_d}\right) - 1 \right]^{-1} \Omega_\lambda d\lambda}{\int_\lambda S_\lambda^{CK} \Omega_\lambda d\lambda} \quad (4)$$

where h is the Planck constant, k_B , the Boltzmann constant and c the speed of light in the vacuum.

Fig. 8 displays the geometric albedo in the *Kepler* bandpass as a function of the brightness temperature of the planet as derived from the previous equations. We found that the thermal emission of the planet is negligible within the *Kepler* bandpass and we found a geometric albedo of $A_g = 0.3 \pm 0.08$. Using this range of values for the albedo and assuming that the geometric albedo related to the Bond albedo through the relation: $A_B = 2/3 A_g$ for a perfect Lambertian sphere (e.g. Rowe et al. 2006), and assuming that the energy redistribution is not efficient ($\varepsilon = 0$) for such a strongly irradiated planet, we estimated the day-side temperature of the planet of $T_{day} = 1930 \pm 80$ K.

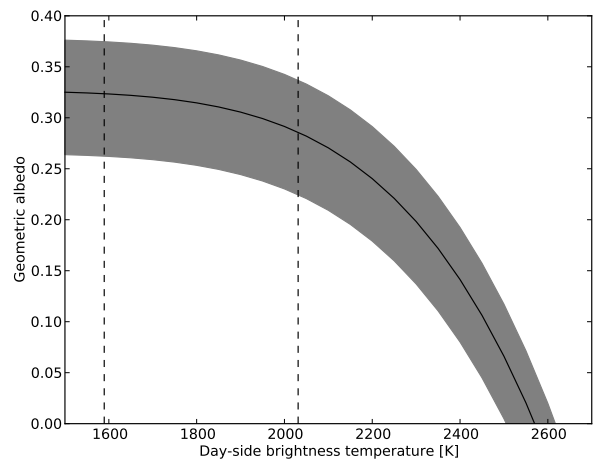


Fig. 8. Geometric albedo as function of planet day-side brightness temperature. Dashed lines represent the brightness temperature of the planet assuming zero Bond albedo and a perfect heat redistribution, $\varepsilon = 1$; $T = 1590 \pm 60$ K (left) and no thermal circulation in the atmosphere $\varepsilon = 0$; $T = 2030 \pm 60$ K (right). The grey band covers the albedo values allowed by the $1-\sigma$ uncertainty on the occultation depth which is assumed to be the dominant uncertainty.

⁴ http://www.stsci.edu/hst/observatory/cdbs/castelli_kurucz_atlas.html

⁵ <http://keplergo.arc.nasa.gov/CalibrationResponse.shtml>

6. Discussion

6.1. A non-inflated low-mass hot-Jupiter

With an orbital period of 1.85558 ± 7.10^{-6} d, a radius of $0.841 \pm 0.032 R_{\text{Jup}}$ and a mass of $0.49 \pm 0.09 M_{\text{Jup}}$, KOI-196b is one of the rare objects with a very short orbital period ($P < 2$ d) and radius and mass smaller than Jupiter. Fig. 9 shows KOI-196 compared with other planets in terms of orbital period, planetary radius and mass. Only HD212301b (Lo Curto et al. 2006) exhibits similar characteristics in terms of mass and orbital period. However as the orbital inclination of this planet is still unknown, the true mass of HD212301b could be likely much higher. Using tables in Fortney et al. (2007), we estimated that the core mass of KOI-196b possesses between $50 M_{\oplus}$ and $100 M_{\oplus}$ of heavy elements. This means that between $\sim 1/3$ and $\sim 2/3$ of KOI-196b’s mass is concentrated in its core. Another high-density short-period planet with radius smaller than Jupiter’s one is HD149026b (Sato et al. 2005). Out of the 141 transiting planets discovered so far, only KOI-196b and HD149026b are located in the hot-Jupiter desert with orbital period shorter than 3 days and with radius or mass smaller than Jupiter. This desert could not be explained by an observational bias since their short orbital periods make their detection easier. These two objects might share the same formation and/or evolution process (Broeg & Wuchterl 2007).

Fig. 10 displays the planetary radius as function of the maximum day-side temperature assuming no heat circulation (i.e. $T_{\text{day}}^{\text{max}} = T_{\text{eff}} / \sqrt{a/R_{\star}}$). There is a clear correlation between the radius and the expected maximum day-side temperature for hot-Jupiters less massive than $2 M_{\text{Jup}}$ as expected theoretically (Burrows et al. 2007; Liu et al. 2008). Once again, in the Saturn-Jupiter domain, KOI-196b and HD149026b appear to be outliers. This might be explained by an unusual high Bond albedo in comparison with other transiting planets as it is observed for KOI-196b. Indeed, it is expected that planets with a higher albedo are cooler (see eq. 3) and thus, are less inflated (see Fig. 10).

High mass-loss can explain this unusual low mass and low radius for a such short-period hot-Jupiter (Ehrenreich & Désert 2011). Using eq. 15 and 22 in Lecavelier Des Etangs (2007) and assuming a efficient extraction of the gas by the extreme ultraviolet incident flux $\eta = 1$, we estimate a current escape rate for KOI-196b of $\sim 0.0005 M_{\text{Jup}} / \text{Gyr}$. Thus, mass-loss is a very unlikely process to explain the low mass and small radius of KOI-196b.

Further studies of internal structure, taking the high albedo of KOI-196b into account, are required to explain the small radius for this close-in planet.

6.2. A high albedo for a hot-Jupiter

KOI-196b is the third hot Jupiter, discovered so far with a such high albedo. The first ones were *Kepler-7b* (Latham et al. 2010) with $A_g = 0.32 \pm 0.03$ (Kipping & Bakos 2011; Demory et al. 2011) and HAT-P-7b (Pál et al. 2008) with an albedo of $A_g = 0.58 \pm 0.05$ (Welsh et al. 2010). Other giant planets with an observed occultation have a very low albedo in the optical $A_B \lesssim 0.1$ (Cowan & Agol 2011). Theoretical studies previously predicted the low-albedo of close-in planets (e.g. Sudarsky et al. 2000) due to the high opacity of Na and K at optical wave-

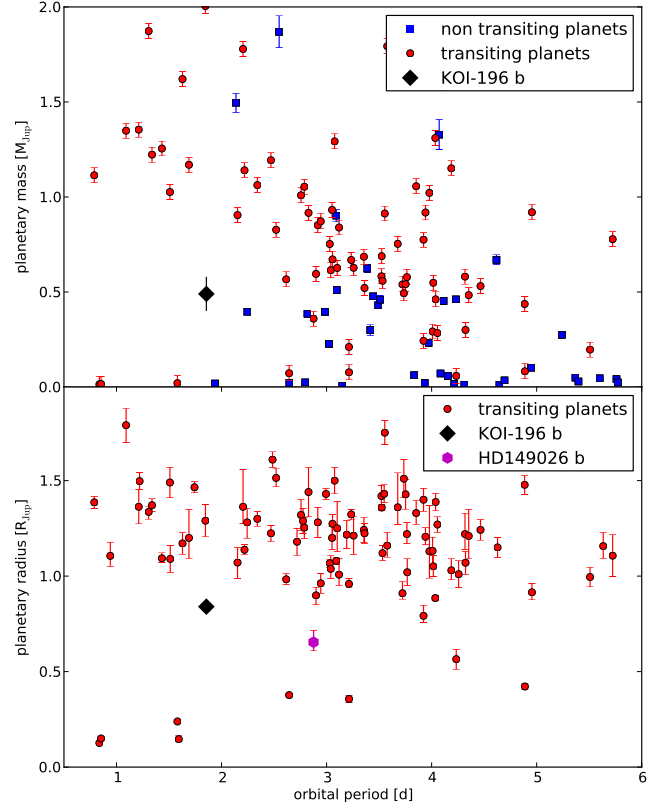


Fig. 9. Planetary mass (upper panel) and radius (lower panel) as a function of orbital period for exoplanets with orbital period less than 6 days (source: Wright et al. 2011). Transiting exoplanets are the red circles and RV planets are the blue squares. We note that for non-transiting planets, the minimum $M \sin i$ is represented here. KOI-196b is marked by a black diamond and HD149026b is marked with a magenta hexagon.

lengths. Demory et al. (2011) suggested that a depletion of such elements in the high atmosphere of *Kepler-7b* compared to solar abundances can explain its high albedo. Sudarsky et al. (2000) have shown that a high albedo can also be explained by the presence of silicate layer high in the atmosphere. Finally, synthetic spectra of the thermal emission of hot-Jupiters from Fortney et al. (2008) suggests that thermal emission could be significantly different from a blackbody emission in the optical. In that case, contribution of the thermal light in the *Kepler* bandpass can be significantly higher, leading to a lower value of the geometric albedo of KOI-196b. Infrared observations of the secondary eclipse and, if possible, the thermal phase variation of KOI-196b are needed to constrain the day-side and night-side temperature as well as to constrain unambiguously its geometric albedo and heat circulation (Cowan & Agol 2011).

7. Conclusion

Thanks to publicly-available *Kepler* photometry and new high-resolution SOPHIE spectroscopic observations, we established the planetary nature of the Kepler Object of Interest KOI-196.01, now called “KOI-196b”, one of the 1235 *Kepler*’s candidates published by Borucki et al. (2011). KOI-196b is a $0.49 \pm 0.09 M_{\text{Jup}} - 0.841 \pm 0.032 R_{\text{Jup}}$ hot-Jupiter orbiting a

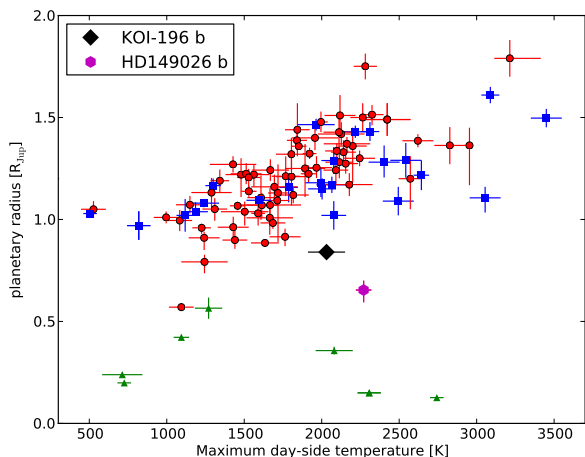


Fig. 10. Planetary radius vs estimated maximum day-side temperature assuming no heat circulation for all transiting planet (source: Wright et al. 2011). Transiting planets with mass $M_p > 2 M_{Jup}$ are the blue squares. Transiting planets with mass in between $M_p = 0.1 M_{Jup}$ and $M_p = 2 M_{Jup}$ are the red circles. Transiting hot-Neptunes and Super-Earths are the green triangles. KOI-196b is marked by a black diamond and HD149026b is marked with a magenta hexagon.

slightly metal-poor G2V star in a $1.855558 \pm 0.000007d$ period. This planet is one of the rare close-in hot-Jupiters with a radius and mass lower than Jupiter suggesting that it is a non-inflated planet. We note that only 6 *Kepler* candidates with priority 2, including KOI-196b, are expected to be hot-Jupiters with an orbital period shorter than 3 days and radius in between $0.5 R_{Jup}$ and $0.9 R_{Jup}$: KOI-102.01, KOI-183.01, KOI-356.01, KOI-801.01 and KOI-883.01. Focusing follow-up efforts on them can help to specify the boundary of the short-period low mass and small radius hot-Jupiter desert, if exists.

Using the high-quality and long time-series of the *Kepler* data, we detected the occultation as well as the optical phase variation of KOI-196b, orbiting a quite faint star ($m_V \sim 14.6$). From the occultation depth and assuming a blackbody planetary thermal emission in the *Kepler* bandpass, we estimated a geometric albedo of the planet to be 0.30 ± 0.08 , which is markedly higher than the geometric albedos observed for most of the known hot-Jupiters (Cowan & Agol 2011). This leads to a day-side temperature of $T_{day} = 1930 \pm 80$ K assuming no thermal redistribution in the atmosphere. Lower values for the albedo are still possible but would indicate a significant contribution of the planetary thermal emission in the optical. This can be unambiguously confirmed with infrared observations of the planetary occultation.

This detection demonstrates once again the efficiency of SOPHIE, a dedicated instrumentation on a 2-m class telescope for the ground-based follow-up of space mission like *Kepler*, *CoRoT* or the ESA M-class mission *PLATO*, if selected.

Acknowledgements. We thank the technical team at the Observatoire de Haute-Provence for their support with the SOPHIE instrument and the 1.93-m telescope and in particular the essential work of the night assistants. We are grateful to the *Kepler* Team for giving public access to the corrected *Kepler* light curve and for publishing a list of good planetary candidates to follow-up. Financial support for the SOPHIE observations from the Programme National de Planétologie (PNP) of CNRS/INSU, France is gratefully acknowledged. We also acknowledge sup-

Table 3. SOPHIE measurements of KOI-196.

BJD (-2 454 900)	RV [km s^{-1}]	$\pm 1\sigma_{rv}$ [km s^{-1}]	V_{span} [km s^{-1}]	S/N/pix @550nm
746.63646	-27.063	0.017	-0.013	16.8
749.65408	-27.141	0.016	0.009	17.0
750.65676	-27.024	0.025	-0.007	14.7
760.60669	-27.110	0.018	-0.035	17.5
761.61891	-27.005	0.015	0.026	19.1
768.62681	-27.130	0.027	-0.033	14.3
769.63221	-26.998	0.018	-0.022	19.3
770.62035	-27.053	0.021	0.022	16.6
854.48407	-27.005	0.024	-0.015	13.7
868.45141	-27.169	0.019	-0.051	16.8
871.45738	-26.957	0.025	0.021	17.4
872.59440	-27.082	0.020	-0.009	17.9

port from the French National Research Agency (ANR-08-JCJC-0102-01). A.S. is grateful to Cilia Damiani for all the fruitful discussions. A.S.B. is supported by CNES.

References

- Alonso, R., Guillot, T., Mazeh, T., Aigrain, S., Alapini, A., Barge, P., Hatzes, A., & Pont, F. 2009a, *A&A*, 501, L23
- Alonso, R., Alapini, A., Aigrain, S., et al. 2009b, *A&A*, 506, 353
- Baglin, A., Auvergne, M., Boisnard, L., et al. 2006, 36th COSPAR Scientific Assembly, 36, 3749
- Baranne, A., Queloz, D., Mayor, M., et al. 1996, *A&AS*, 119, 373
- Batalha, N. M., Rowe, J. F., Gilliland, R. L., et al. 2010, *ApJ*, 713, L103
- Batalha, N., Borucki, W., Bryson, S., et al. 2011, *ApJ*, 729, 27
- Boisse, I., Eggenberger, A., Santos, N. C., et al. 2010, *A&A*, 523, A88
- Bonomo, A. S., Santerne, A., Alonso, R., et al. 2010, *A&A*, 520, A65
- Borucki, W. J., Koch, D., Jenkins, J., et al. 2009, *Science*, 325, 709
- Borucki, W. J., Koch, D. G., Brown, T. M., et al. 2010a, *ApJ*, 713, L126
- Borucki, W. J., Koch, D. G., Basri, G., et al. 2010b, *Science*, 327, 977
- Borucki, W. J., Koch, D. G., Basri, G., et al. 2011, *ApJ*, 736, 19
- Bouchy, F., Isambert, J., Lovis, C., Boisse, I., Figueira, P., Hébrard, G., & Pepe, F. 2009a, *EAS Publications Series*, 37, 247
- Bouchy, F., Moutou, C., Queloz, D., & the *CoRoT* Exoplanet Science Team 2009b, *IAU Symposium*, 253, 129
- Bouchy, F., Hébrard, G., Udry, S., et al. 2009c, *A&A*, 505, 853
- Bouchy, F., Bonomo, A. S., Santerne, A., et al. 2011, *A&A*, in press, arXiv:1106.3225
- Broeg, C., & Wuchterl, G. 2007, *MNRAS*, 376, L62
- Bruntt, H., Catala, C., Garrido, R., et al. 2002, *A&A*, 389, 345
- Bruntt, H., De Cat, P., & Aerts, C. 2008, *A&A*, 478, 487
- Bruntt, H., Deleuil, M., Frindlund, M., et al. 2010, *A&A*, 519, A51
- Burrows, A., Hubeny, I., Budaj, J., & Hubbard, W. B. 2007, *ApJ*, 661, 502
- Cardelli, J. A., Clayton, G. C., & Mathis, J. S. 1989, *ApJ*, 345, 245
- Casagrande, L., Ramírez, I., Meléndez, J., Bessell, M., & Asplund, M. 2010, *A&A*, 512, A54
- Castelli, F., & Kurucz, R. L. 2004, arXiv:astro-ph/0405087
- Cowan, N. B., & Agol, E. 2011, *ApJ*, 729, 54
- Deeg, H. J., Moutou, C., Erikson, A., et al. 2010, *Nature*, 464, 384
- Demory, B.-O., Seager, S., Madhusudhan, N. et al. 2011, *ApJ*, 735, L12
- Ehrenreich, D., & Désert, J.-M. 2011, *A&A*, 529, A136
- Fortney, J. J., Marley, M. S., & Barnes, J. W. 2007, *ApJ*, 659, 1661
- Fortney, J. J., Lodders, K., Marley, M. S., & Freedman, R. S. 2008, *ApJ*, 678, 1419
- Giménez, A. 2006, *A&A*, 450, 1231
- Giménez, A. 2009, The Eighth Pacific Rim Conference on Stellar Astrophysics: A Tribute to Kam-Ching Leung, 404, 291
- Jenkins, J. M., Caldwell, D. A., Chandrasekaran, H., et al. 2010, *ApJ*, 713, L87
- Holman, M. J., Fabrycky, D. C., Ragozzine, D., et al. 2010, *Science*, 330, 51
- Kipping, D. M. 2010, *MNRAS*, 408, 1758
- Kipping, D., & Bakos, G. 2011, *ApJ*, 730, 50
- Latham, D. W., Borucki, W. J., Koch, D. G., et al. 2010, *ApJ*, 713, L140
- Lecavelier Des Etangs, A. 2007, *A&A*, 461, 1185
- Léger, A., Rouan, D., Schneider, J., et al. 2009, *A&A*, 506, 287
- Lissauer, J. J., Fabrycky, D. C., Ford, E. B. et al. 2011, *Nature*, 470, 53
- Liu, X., Burrows, A., & Ibgui, L. 2008, *ApJ*, 687, 1191
- Lo Curto, G., Mayor, M., Clausen, J. V., et al. 2006, *A&A*, 451, 345
- López-Morales, M., & Seager, S. 2007, *ApJ*, 667, L191

- Mardling, R. A. 2007, MNRAS, 382, 1768
- Pál, A., Bakos, G. Á., Torres, G., et al. 2008, ApJ, 680, 1450
- Pepe, F., Mayor, M., Galland, F., et al. 2002, A&A, 388, 632
- Press, W. H., Teukolsky, S. A., Vetterling, W. T., & Flannery, B. P. 1992, Cambridge: University Press, 1c1992, 2nd ed.
- Queloz, D., Henry, G. W., Sivan, J. P., et al. 2001, A&A, 379, 279
- Queloz, D., Bouchy, F., Moutou, C., et al. 2009, A&A, 506, 303
- Perruchot, S., Kohler, D., Bouchy, F., et al. 2008, Proc. SPIE, 7014
- Snellen, I. A. G., de Mooij, E. J. W., & Albrecht, S. 2009, Nature, 459, 543
- Snellen, I. A. G., de Mooij, E. J. W., & Burrows, A. 2010, A&A, 513, A76
- Turck-Chièze, S., Palacios, A., Marques, J. P., & Nghiem, P. A. P. 2010, ApJ, 715, 1539
- Rowe, J. F., Matthews, J. M., Seager, S., et al. 2006, ApJ, 646, 1241
- Santerne, A., Díaz, R. F., Bouchy, F., et al. 2011, A&A, 528, A63
- Sato, B., Fischer, D. A., Henry, G. W., et al. 2005, ApJ, 633, 465
- Sing, D. K. 2010, A&A, 510, A21
- Sudarsky, D., Burrows, A., & Pinto, P. 2000, ApJ, 538, 885
- Torres, G., Fressin, F., Batalha, N. M., et al. 2011, ApJ, 727, 24
- Welsh, W. F., Orosz, J. A., Seager, S., Fortney, J. J., Jenkins, J., Rowe, J. F., Koch, D., & Borucki, W. J. 2010, ApJ, 713, L145
- Wright, J. T., Fakhouri, O., Marcy, G. W., et al. 2011, PASP, 123, 412